Dechanneling by dislocations in ion-implanted Al

S. T. Picraux
Sandia Laboratories, Albuquerque, New Mexico 87185

E. Rimini, G. Foti, and S. U. Campisano
Istituto di Struttura della Materia, Corso Italia 57, Catania, Italy

(Received 14 February 1978)

The first comprehensive ion-backscattering study of the influence of dislocations on the dechanneling of energetic channeled ions has been carried out. High dislocation densities were obtained in the near-surface region of single-crystal Al by implantation of 6.6×10^{16} Al/cm^2 or 2.6×10^{16} Zn/cm^2. Independent analysis of the disorder introduced by the Al and Zn implantations, as well as a quantitative measure of the total length of dislocation lines per cm^2, were obtained by transmission-electron microscopy. Dechanneling measurements were made by means of ion backscattering for H^+ and He^+ ions ranging in energy from 0.5 to 2.8 MeV, incident along the ⟨110⟩ axial and {111} planar channeling directions. For these experimental parameters a systematic dependence of the dechanneling versus depth is demonstrated. These experimental observations are characteristic of that predicted theoretically for dechanneling by dislocations and distinctly different from that observed for randomly displaced atoms. The theoretical analysis for the data reduction is developed to obtain the dechanneling cross section for dislocations from the experimental data for both axial and planar channeling. The results are in agreement with independent theoretical calculations of the dislocation dechanneling cross section by Quéré, both quantitatively and in the functional dependences of the dechanneling parameter on energy, ion type, and channeling direction. From these studies the measurement of dislocation density by single alignment channeling is estimated to require 10^9–10^{10} dislocation lines per cm^2. Although axial channeling has been used in the past for depth profiling measurements of disorder by backscattering, the large dechanneling cross sections and well-defined dechanneling behavior shown here for planar channeling suggest that planar analysis may be more suitable than axial for determining the depth distribution of dislocations by channeling-effect measurements.

I. INTRODUCTION

Ion channeling, in conjunction with ion backscattering measurements, has been used extensively to study disorder in the near-surface region of single crystals. For a channeled beam of ions a spatial redistribution of the incident-ion probability density occurs, such that there is a very low probability to find a channeled particle closer than approximately the Thomas-Fermi screening distance to the atom rows or planes ($\simeq 0.1$–0.2 Å) and a high probability for channeled ions outside this region. Thus the channeling technique can be used to detect the number of atoms which are displaced >0.1 Å away from lattice positions. Usually the direct scattering by displaced atoms is used to obtain a measure of the disorder and the dechanneled component is subtracted as a background. Channeling has been used in this way to carry out extensive studies of implantation disorder in ion-implanted semiconductors.[1,2]

However, a major difficulty arises in the quantitative analysis of channeling data if the distribution of displaced atoms is not approximately uniform across the channel. In this case the direct scattering and dechanneling signals both depend on the number of displaced atoms and their position. This is because the density of channeled particles and their collision-induced progression towards dechanneled trajectories both vary strongly with lateral position in the channel. In fact, for small atom displacements from rows or planes the direct scattering contribution becomes negligible relative to the dechanneling signal. For this case an accurate interpretation of the dechanneling is required to obtain a quantitative measure of the disorder and its depth distribution.

One approach to better understand and develop the channeling technique for the analysis of disorder which gives rise primarily to dechanneling has been to select model systems where one type of disorder predominates. Then systematic channeling studies are carried out, preferably in conjunction with an independent measurement of the disorder, for quantitative interpretation. In this way it has been found that channeling measurements as a function of various experimental parameters can greatly help in understanding the nature of the disorder.

In one system small displacements in Si due to light ion implantation have been studied as a function of tilt angle within major channeling directions.[3] Here the direct scattering contribution was still measurable and this was shown to provide information on the radial density of displacements around the crystal rows. A second system in-

volved ion implantation into Au, for which electron microscopy analysis reveals the formation of black spots which are interpreted as small clusters of disordered Au atoms.[4] These studies have emphasized methods of obtaining the depth distribution of disorder without a detailed knowledge of the nature of the clusters giving rise to the black spots. In a third model system detailed studies were carried out on heteroepitaxially-grown Si layers which contained high densities of stacking faults.[5] This case provided a nice example of planar defects and it demonstrated, in conjunction with electron microscopy, how quantitative analysis of such defects could be obtained from the dechanneling distributions. In all the above cases ion backscattering has been used. However, systematic studies have also been carried out in transmission for a variety of cases including interstitials, bubbles, stacking faults, and dislocations.[6]

The present study reports a detailed analysis of the influence of dislocations on the dechanneling behavior of channeled ions. This model system is obtained by the implantation of Al or Zn into Al. The study combines ion backscattering measurements as a function of various channeling parameters with independent measurements of the disorder by transmission-electron microscopy (TEM). Detailed channeling analyses as well as comparison with theory are carried out in order to gain an overall understanding of the influence of the small correlated displacements around dislocations on channeled ions. The objective is to further develop the channeling technique for the quantitative study of this type of disorder. Preliminary results of this study for Zn-implanted Al have been reported in previous conference proceedings.[7,8]

The experimental procedure is presented in Sec. II. In Sec. III the results are given for Al-implanted Al and Zn-implanted Al by ion channeling measurements, and then by transmission electron microscopy measurements. In Sec. IV the dechanneling analysis procedure is given and applied to the present data. This is followed in Sec. V by a discussion of the results and comparison with theory.

II. EXPERIMENTAL PROCEDURE

Aluminum single crystals of ⟨110⟩ orientation were prepared by electropolishing and in some cases were subsequently vacuum annealed at 400 °C. Implantation was carried out at room temperature using a magnetically analyzed and swept ion beam in a vacuum system with base pressure in the 10^{-7}-Torr range. Implantations were carried out along a nonchanneling direction 12°–15° from the ⟨110⟩ axis with an average beam intensity of $1\,\mu A/cm^2$. The Zn implantations were carried out at an incident energy of 200 keV to a fluence of 2.6×10^{16} Zn/cm^2, and the Al implantations were carried out at 85 keV to a fluence of 6.6×10^{16} Al-cm^2.

Channeling effect measurements were performed for H^+ and He^+ ion backscattering at 165° in the energy range 0.5–2.8 MeV. Analysis was carried out along the ⟨110⟩ axial direction and {111} planar direction, both of which were normal to the sample surface. TEM measurements were done at 100 keV in samples which were thinned prior to implantation. They were implanted under the same conditions as for the channeling analysis, except that the sample surface was tilted 45° from the beam normal to restrict the depth of the implanted damage to that which could be observed in the microscope.

III. RESULTS

A. Al(Al) channeling

In Fig. 1 He backscattering spectra are shown for channeling along the ⟨110⟩ axial direction in Al-implanted Al for (a) 1.0-, (b) 1.5-, and (c) 2.0-MeV incident He^+ ions. The reduction in scattering relative to the random spectrum is seen to decrease with increasing He beam energy. In each figure the curve labeled *virgin* gives the channeled energy spectrum for the same crystal in an unimplanted region. Below the surface peak there is an increase in the channeling signal with decreasing energy. This dechanneling is initially greater than that of the virgin crystal and is gradually reduced at decreasing energy (increasing depths) until the dechanneling rate is approximately equal to that for the virgin crystal. This similar dechanneling rate is indicated by the equal slopes of the channeled spectra in Fig. 1 and is most apparent for the highest energy analysis. In general a dechanneling rate equal to that for the virgin crystal indicates a region of undistorted single crystal material. As will be discussed later, the observed spectra are consistent with a calculated[9] projected range for 85-keV Al in Al of ≈ 1100 Å and a range spread of ≈ 400 Å.

The information contained in the channeled spectra can be compared for the different energies by plotting the results in terms of the dechanneled fraction (the ratio of aligned-to-random yield) as a function of depth, where the backscattered particle energy scale has been converted into a depth scale using conventional energy-loss parameters.[10] The resulting dechanneling curves are shown in Fig. 2 for the data of Fig. 1 for (a)

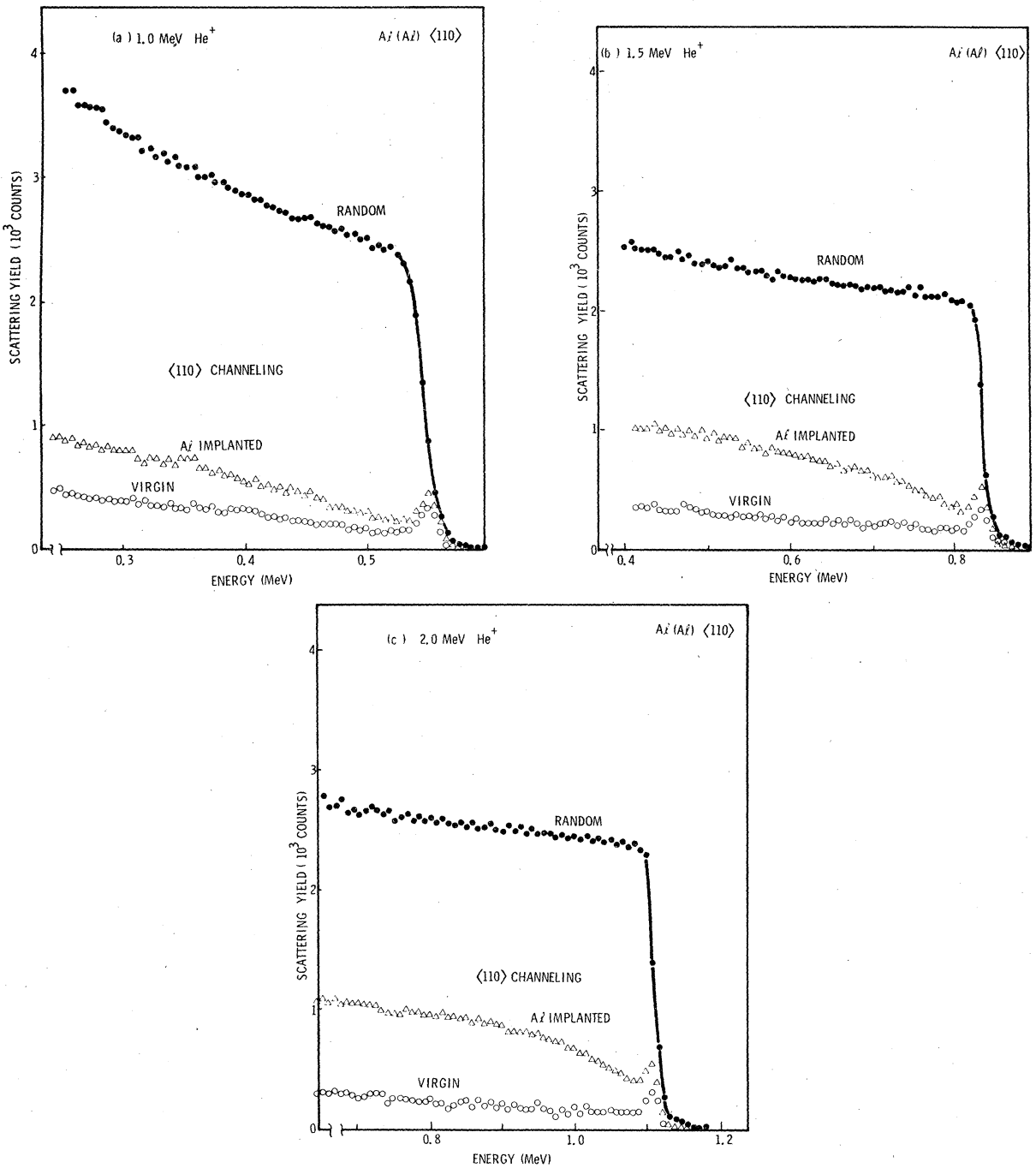

FIG. 1. The ⟨110⟩ channeled and randon backscattering spectra from unimplanted (virgin) and 85-keV Al-implanted Al crystals for incident He beam energies (a) 1.0, (b) 1.5, and (c) 2.0 MeV.

virgin and (b) Al-implanted Al. The dechanneled fraction is appreciably greater in the implanted crystal, indicating the presence of appreciable disorder in the near-surface region. Even more striking is the reversal of the energy dependence, such that the dechanneled fraction increases with increasing analyzing beam energy for the implanted sample, whereas the intrinsic dechanneling mechanisms in an undamaged crystal lead to a decrease in channeling with increasing incident energy. In Fig. 3 the channeled spectra are seen to exhibit the same energy dependence for proton analysis,

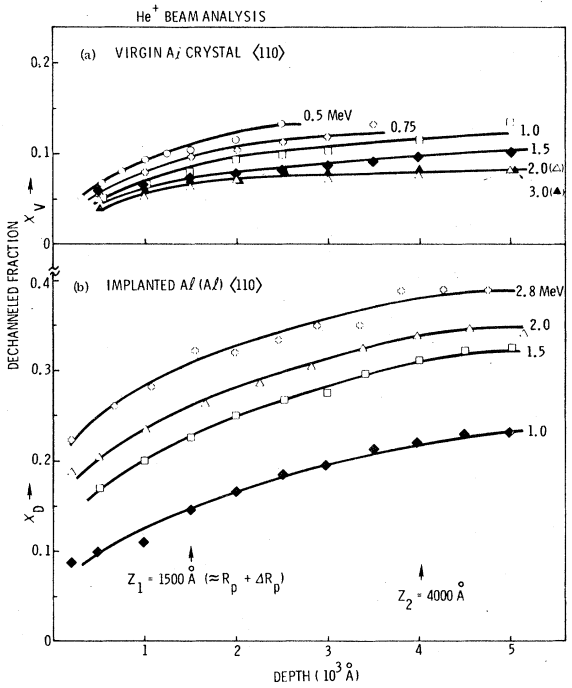

FIG. 2. Dechanneled fraction vs depth for the ⟨110⟩ axial channeling as a function of incident He beam energy for (a) virgin Al and (b) Al-implanted Al.

where ⟨110⟩ spectra are shown for the same Al-implanted Al sample for incident proton energies of (a) 0.5, (b) 0.75, and (c) 1.0 MeV.

From the energy dependence of these data we can conclude that the dechanneling is not primarily associated with randomly displaced atoms, as is commonly observed in implanted semiconductors. We demonstrate this directly for an Al-implanted Al system by evaporating a thin Al film (thickness $\simeq$ 1100 Å) on one of the ⟨110⟩ Al single-crystal surfaces. The resulting polycrystalline film represents a layer of scattering centers which are essentially randomly located with respect to the underlying ⟨110⟩ rows. In Fig. 4 examples of the backscattering spectra for ⟨110⟩ aligned and random substrate orientation are shown at two incident He energies. The Al grains in the film are seen to be misaligned with respect to the ⟨110⟩ substrate direction since the channeling yield is the same as the random yield over an energy region corresponding to the thickness of the film. Be measuring the channeled minimum yield after passing through the film as a function of incident He energy, as indicated by the ratio of H_a/H_r in Fig. 4, one can compare the random scattering film and implanted disorder cases, in each case for a monoatomic Al system.

Results for the Al film and Al implant are shown in Fig. 5, where the minimum yield is plotted vs the reciprocal of the incident beam energy for He channeling along the ⟨110⟩ axis. In each case the minimum yield has been measured at a depth of 1100 Å. The influence of randomly distributed scattering centers on channeling is well understood[11] and the solid line in Fig. 5 for the Al film was calculated as follows. The angular distribution of the particles after passing through the Al film is obtained using the plural scattering theory[12] (where here the mean number of collisions or effective thickness is $m = 6.4$), and all particles with angle greater than the critical angle are considered to be dechanneled and therefore contribute to the minimum yield. The calculated full line in Fig. 5 is seen to agree very well with the experimental minimum yield data for the thin evaporated Al film. In contrast, a reverse energy dependence is observed for implanted Al, indicating a clear difference in the nature of the disorder from random scattering centers. The theoretical discussion of this dramatically different dependence will be given in Sec. IV.

Planar channeling analysis of the Al-implanted Al crystals shows the same energy dependence as was observed for the axial data. In Fig. 6 are shown the energy spectra for He ions incident along the {111} plane for three different incident energies (a) 0.75, (b) 1.0, and (c) 2.0 MeV. The derived dechanneled fraction vs depth curves are shown for the virgin and implanted Al cases in Figs. 7(a) and 7(b), respectively. The change in planar dechanneled fraction with energy is more pronounced in the planar case than in the axial case. Again the energy dependence of the dechanneling is observed to be reversed between the virgin and implanted crystals, as was found for the axial dechanneling. In addition, the change from rapid dechanneling in the near-surface region to a flat dependence at deeper depths is more pronounced for the planar than for the axial channeling measurements.

B. Al(Zn) channeling

To demonstrate that the above results for self-ion implantation are a general feature of ion implantation damage in Al crystals, we have carried out similar measurements for a heavier ion, Zn, implanted into Al. A Zn implantation energy of 200 keV was chosen in order to maintain approximately the same theoretical projected range ($\approx$ 1100 Å) and range spread ($\approx$ 400 Å) as for the 85-keV Al implants. The Zn implantation fluence was reduced by a factor of approximately 2.5 to the value $2.6 \times 10^{15}/\text{cm}^2$; this corresponds to the ratio of the theoretically predicted energy deposition into atomic collision processes for 200-keV Zn relative

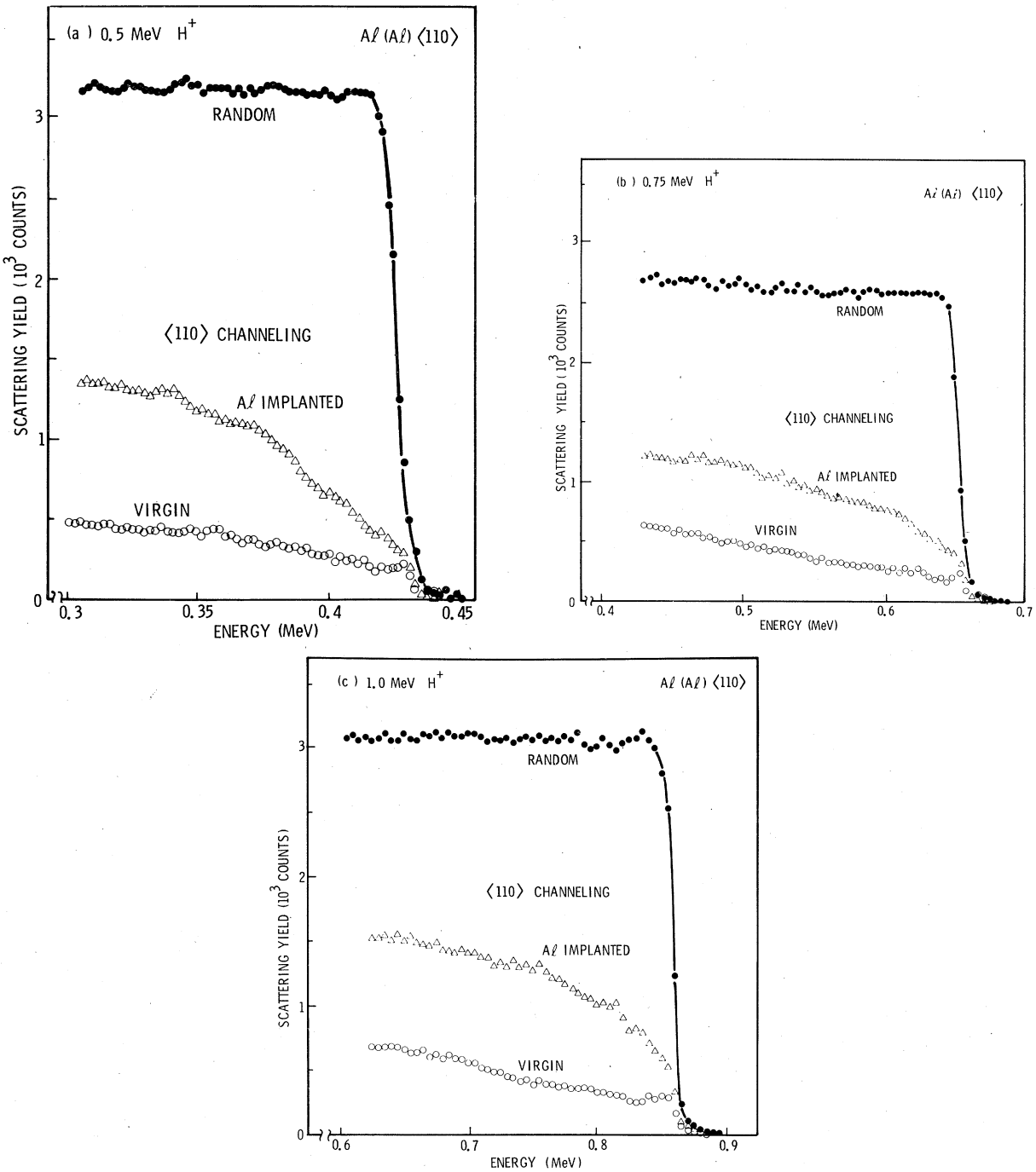

FIG. 3. The ⟨110⟩ axial channeled and random backscattering spectra for protons incident on virgin Al and Al-implanted Al at (a) 0.5, (b) 0.75, and (c) 1.0 MeV.

to 85-keV Al. Therefore, the total energy deposited into damage production was also the same for the two implants. Thus, aside from differences resulting from the higher energy density in the Zn ion damage cascade, the resulting amount of disorder should be comparable for the Al and Zn implants, and this was observed to be the case.

The results for the energy dependence of the He channeling along ⟨110⟩ axial and {111} planar directions are presented in Figs. 8 and 9, respectively. The same general behavior is observed for the dechanneled fraction versus depth, both

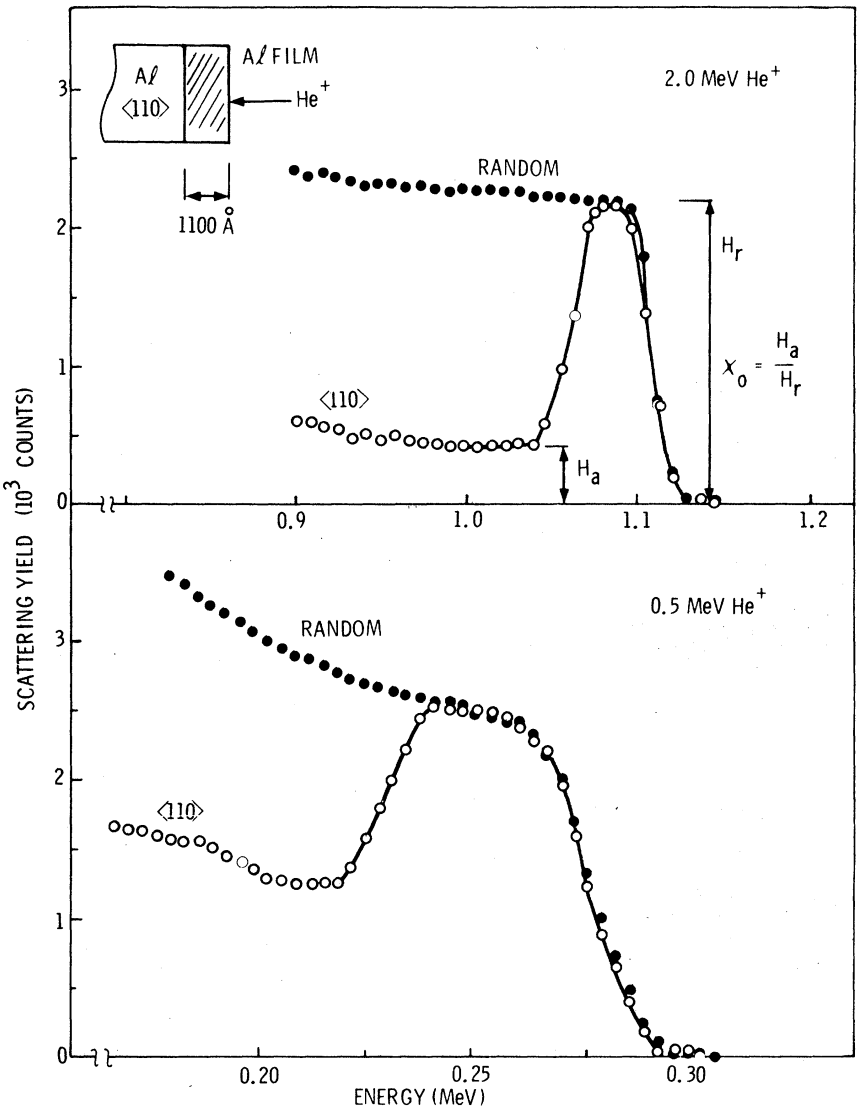

FIG. 4. The ⟨110⟩ axial channeled and random backscattering spectra for He incident at 2.0 (upper part) and 0.5 MeV (lower part) onto a 1100-Å Al vapor-deposited film on a ⟨110⟩ oriented Al substrate.

in terms of the energy dependence of the dechanneling and the depth over which the more rapid change in dechanneling occurs. In addition, in Fig. 10 the angular distributions for 2-MeV He channeling along the ⟨110⟩ axis are compared for the Zn-implanted versus unimplanted Al case. The relative yield represents the average value over the first 2000 Å in depth. An increase in the minimum yield is observed for the implanted sample, consistent with the data of Fig. 8, and the decrease in the shoulder region (near ±1°) is also consistent with the presence of disorder. There is little difference, however, in the critical angle, with only about a 2% increase in the half-angle for the damaged crystal over that for the virgin crystal. These results suggest that little additional information can be gained from the angular distribution measurements for this model system and therefore further angular distribution measurements were not made.

C. Transmission-electron-microscopy results

A dark field micrograph for the Al implant is shown in Fig. 11 and reveals the presence of a very dense, tangled network of dislocation lines present in the implanted material. The same qualitative behavior is observed for the Zn implants, and a similar micrograph for this case is shown in Fig. 12. The thickness of the analyzed region is esti-

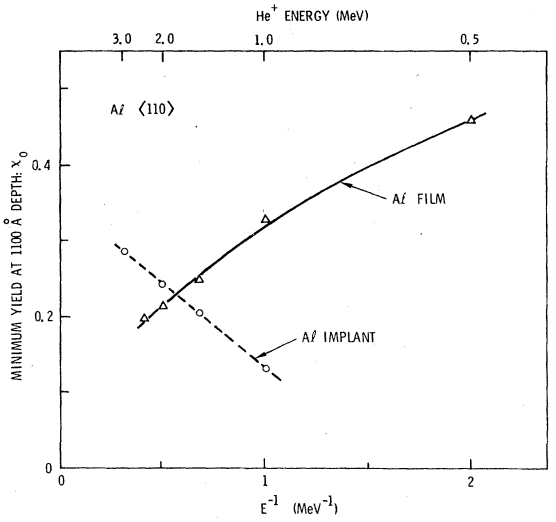

FIG. 5. Minimum yield measured at a depth of 1100 Å vs reciprocal He beam energy for the Al film and Al-implanted Al. Solid line is theoretical prediction for randomly located scattering centers and dashed line is fit to Al implant data.

mated to be ~1000 Å. This is believed to include the major part of the damaged region since for the TEM samples the projected range was reduced by ≈70% to 780 Å by tilting the target 45°. Although the dislocation density is high for analysis by TEM, we have been able to make approximate measurements of the total length of dislocation lines per unit area. The measured projected length is corrected for the difference in tilt of the sample during implantation between the TEM and channeling samples, and also for the number of dislocations out of contrast for the imaging conditions used. The resulting projected dislocation line length for comparison to the channeling data is 9.6×10^5 cm/cm^2 for the Zn implant and 1.6×10^6 cm/cm^2 for the Al implant. The absolute accuracy of these dislocation length measurements is estimated to be within a factor of 2 and is primarily limited by the overlapping strain fields of the dense dislocation network.

In Fig. 13 is shown the diffraction patterns for a ⟨110⟩ pole direction for (a) virgin Al, (b) Al-implanted Al, and (c) Zn-implanted Al. From comparison of these diffraction patterns, which are indistinguishable within the resolution of these measurements, we conclude that any mosaic spread induced by the implantation, if present, is sufficiently small (<0.5°) to have negligible influence on the channeling data. In addition, the diffraction data indicate that no new phases have been induced in the samples by implantation. This would be expected for a pure Al implantation into Al, since no other chemical species are present,

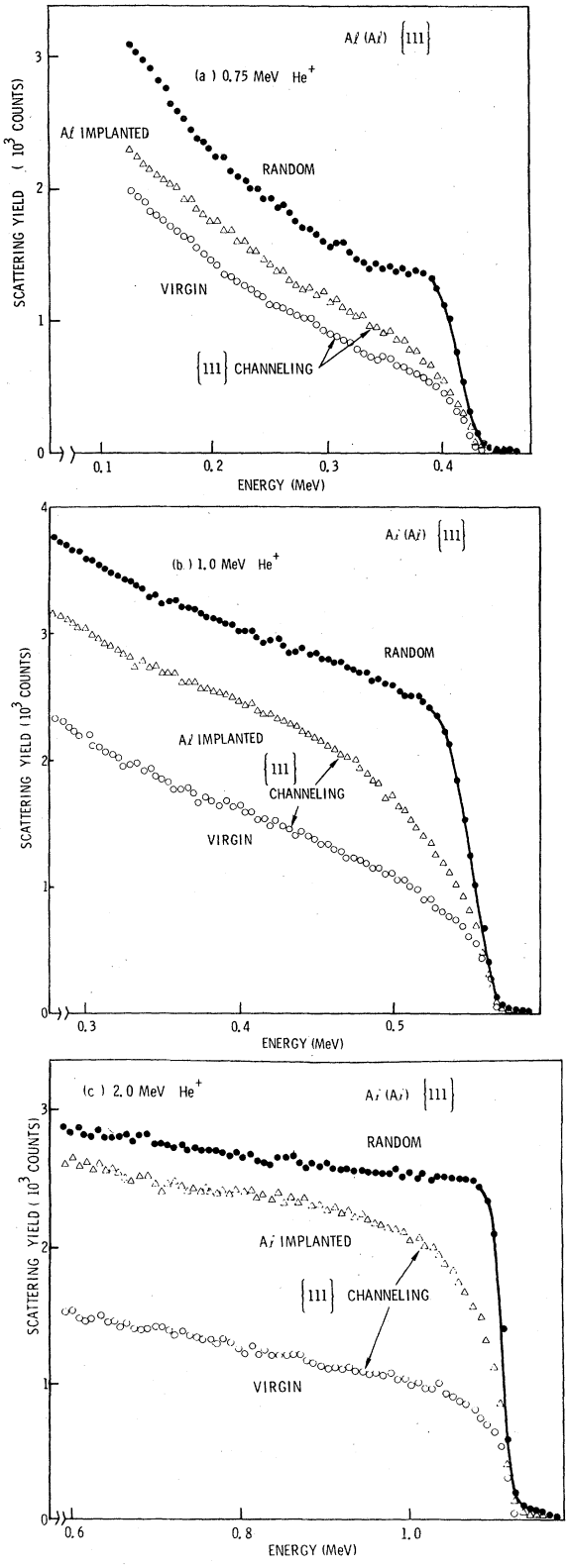

FIG. 6. The {111} planar channeled and random backscattering spectra for a He beam incident on virgin Al and Al-implanted Al at (a) 0.75, (b) 1.0, and (c) 2.0 MeV.

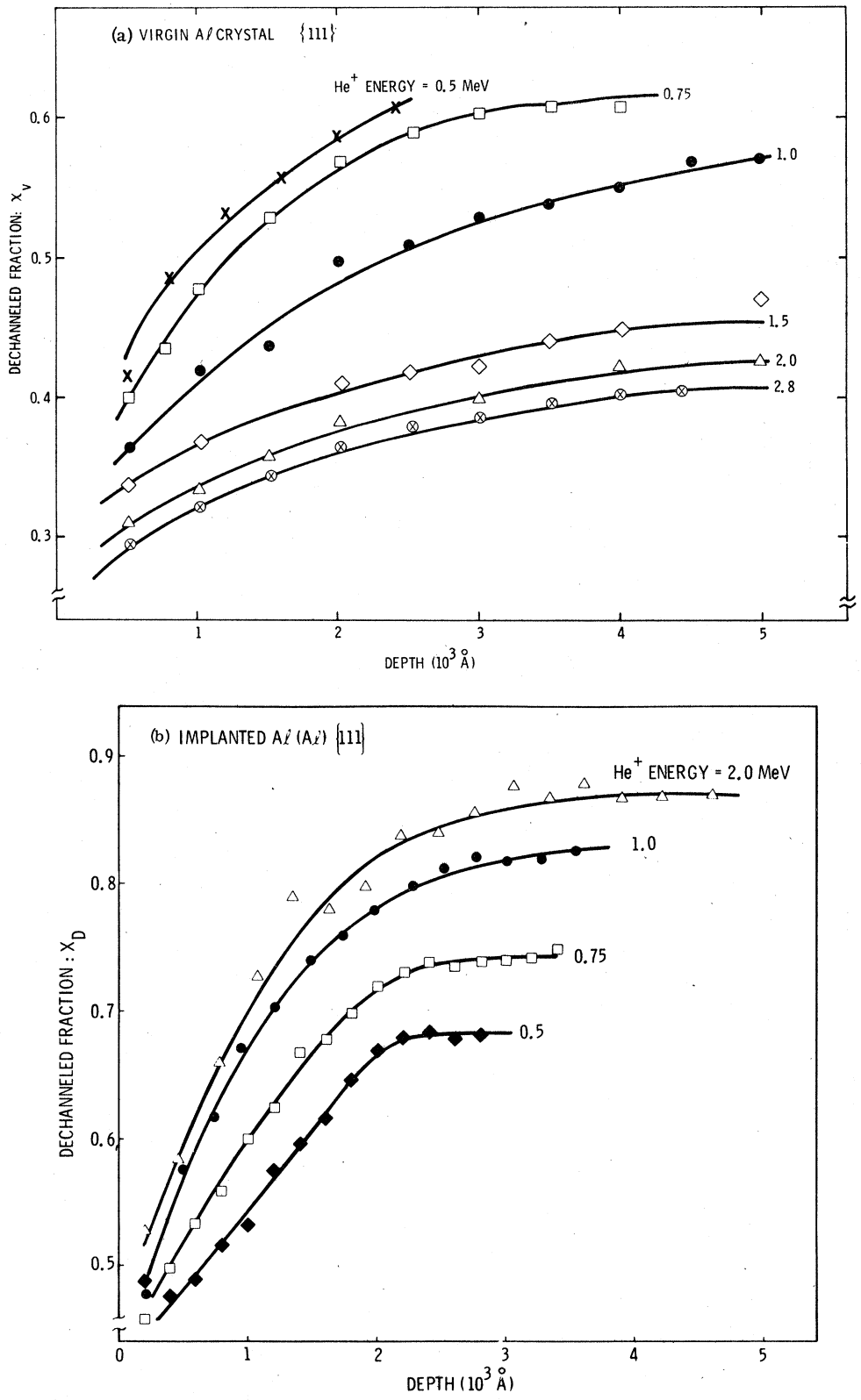

FIG. 7. Dechanneled fraction vs depth for {111} planar channeling as a function of incident He beam energy for (a) virgin Al and (b) Al-implanted Al.

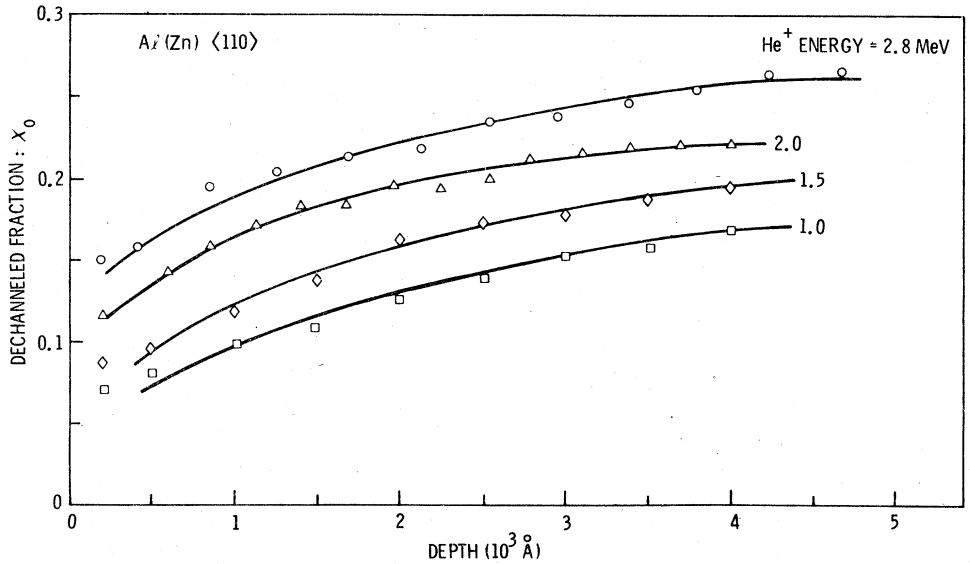

FIG. 8. Dechanneled fraction vs depth for the ⟨110⟩ axis as a function of incident He beam energy for Zn-implanted Al.

and also for the Zn implantation, since the Zn atom mobility should be nil at room temperature and therefore give a randomly dispersed Zn distribution throughout the implanted region.

IV. THEORETICAL ANALYSIS OF RESULTS

The procedure for analysis of disorder in channeling measurements requires a model to describe the

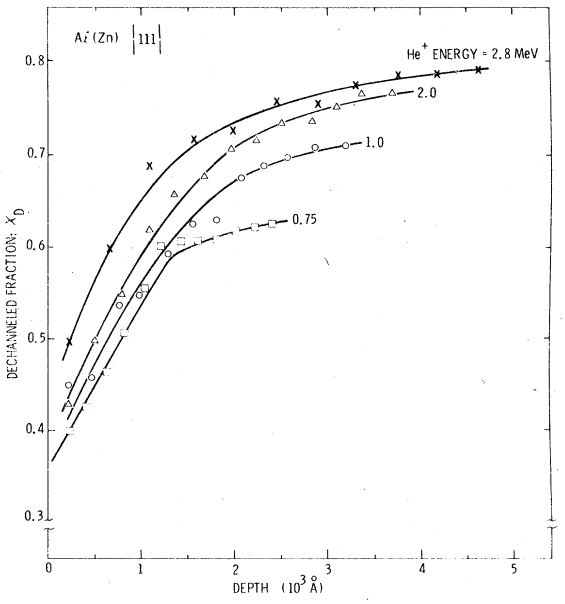

FIG. 9. Dechanneled fraction vs depth for {111} planar channeling as a function of incident He energy for Zn-implanted Al.

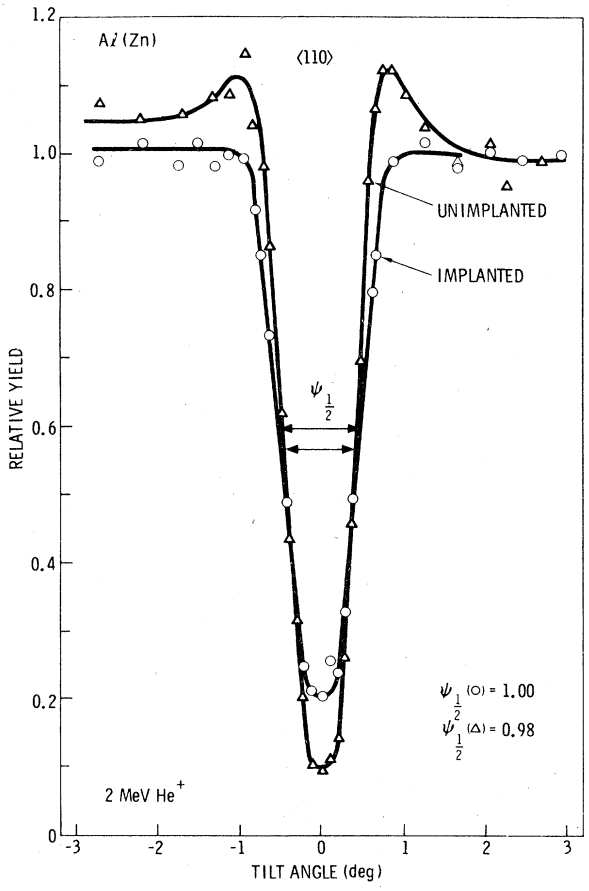

FIG. 10. Channeling ⟨110⟩ angular distributions for 2-MeV He incident on Zh-implanted Al and virgin Al where the relative yield is taken over a depth of the first 2000 Å.

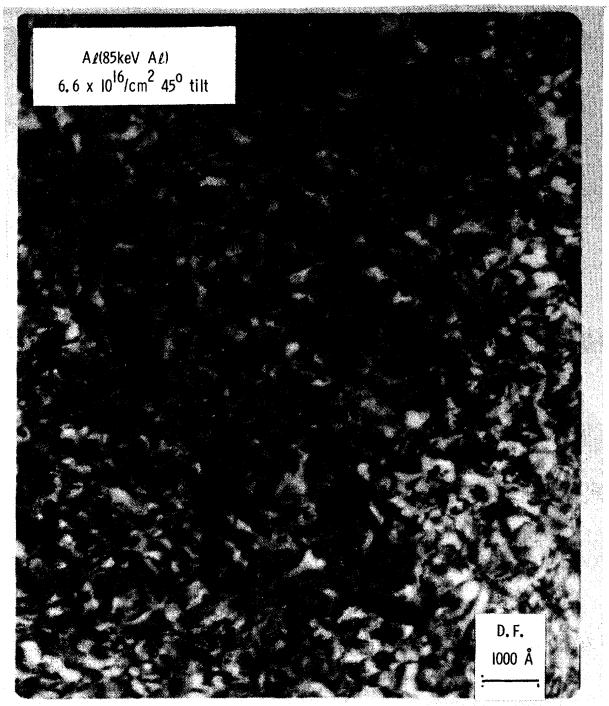

FIG. 11. Dark-field (D.F.) micrograph of Al-implanted Al using $g = [111]$.

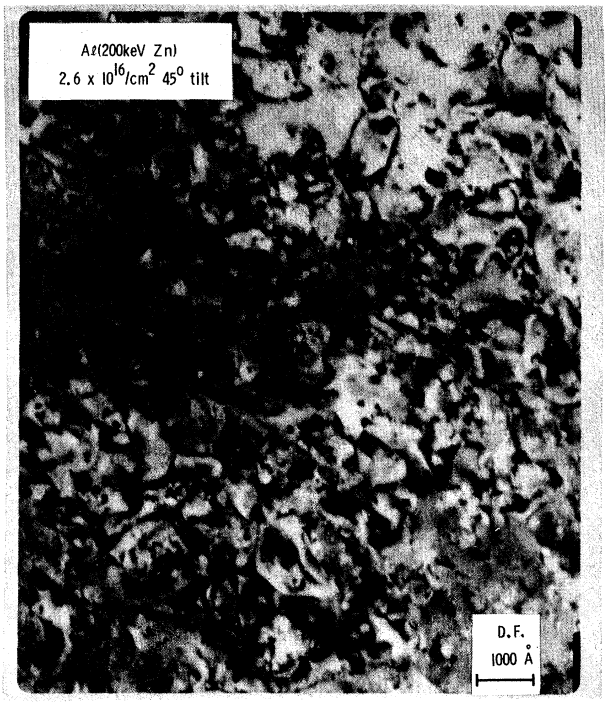

FIG. 12. Dark-field micrograph of Zn-implanted Al using $g = [111]$.

interaction of channeled particles with defects. A standard approach[13] for randomly displaced atoms in the host lattice is usually adopted under several assumptions: (i) dechanneling due to defects is additive to that caused by electrons and thermally vibrating nuclei; (ii) dechanneled particles are not scattered back into channels; and (iii) the critical angle is not changed by the introduction of disorder. As illustrated in Fig. 14(a) the aligned yield normalized by the random yield, χ_D, can be described at depth z in terms of two components;

$$\chi_D(z) = \chi_R(z) + [1 - \chi_R(z)]\, n_D(z)/n, \tag{1}$$

where the first term, χ_R, is the dechanneled fraction of the aligned beam and the second term represents the direct scattering of the channeled fraction of the aligned beam from displaced atoms of density n_D for crystal atom density n. The dechanneled component is given by

$$\chi_R(z) = \chi_V(z) + [1 - \chi_V(z)]\,\{1 - \exp[-\sigma N_D(z)]\}, \tag{2}$$

where χ_V is the aligned yield at depth z for a virgin crystal, σ is the dechanneling cross section for the defects, and $N_D(z)$ is the total number of defects per centimeter^2 integrated from the surface to the depth z. In this analysis the use of χ values measured in virgin crystals implies the assumption of additivity of the various contributions to dechanneling.[14-16]

In the present case, TEM measurements indicate that the disorder is dominated by dislocations. Dechanneling due to an edge dislocation is illustrated schematically in Fig. 14(b). Particles impinging normal to the dislocation line see a disordered axial or planar channel due to the bending of the atomic planes. The interaction of the channeled particles with the strain field surrounding the dislocation line can be approximated in terms of a dechanneling cross section per unit length of dislocation line λ, which may be thought of as an effective width of the dislocation for dechanneling. Consistent with the small displacements of lattice atoms around dislocations, there is negligible contribution to direct scattering relative to the dechanneling and thus, $\chi_D \simeq \chi_R$. This is confirmed by the lack of even a small disorder peak in the vicinity of the implanted region. Therefore from Eq. (2) we obtain

$$1 - \chi_D(z)/1 - \chi_V(z) = \exp[-\lambda L(z)] \tag{3}$$

where $L(z)$ denotes the total length of dislocation lines per centimeter^2 between the surface and depth z,

$$L(z) = \int_0^z l(z')\, dz' \tag{4}$$

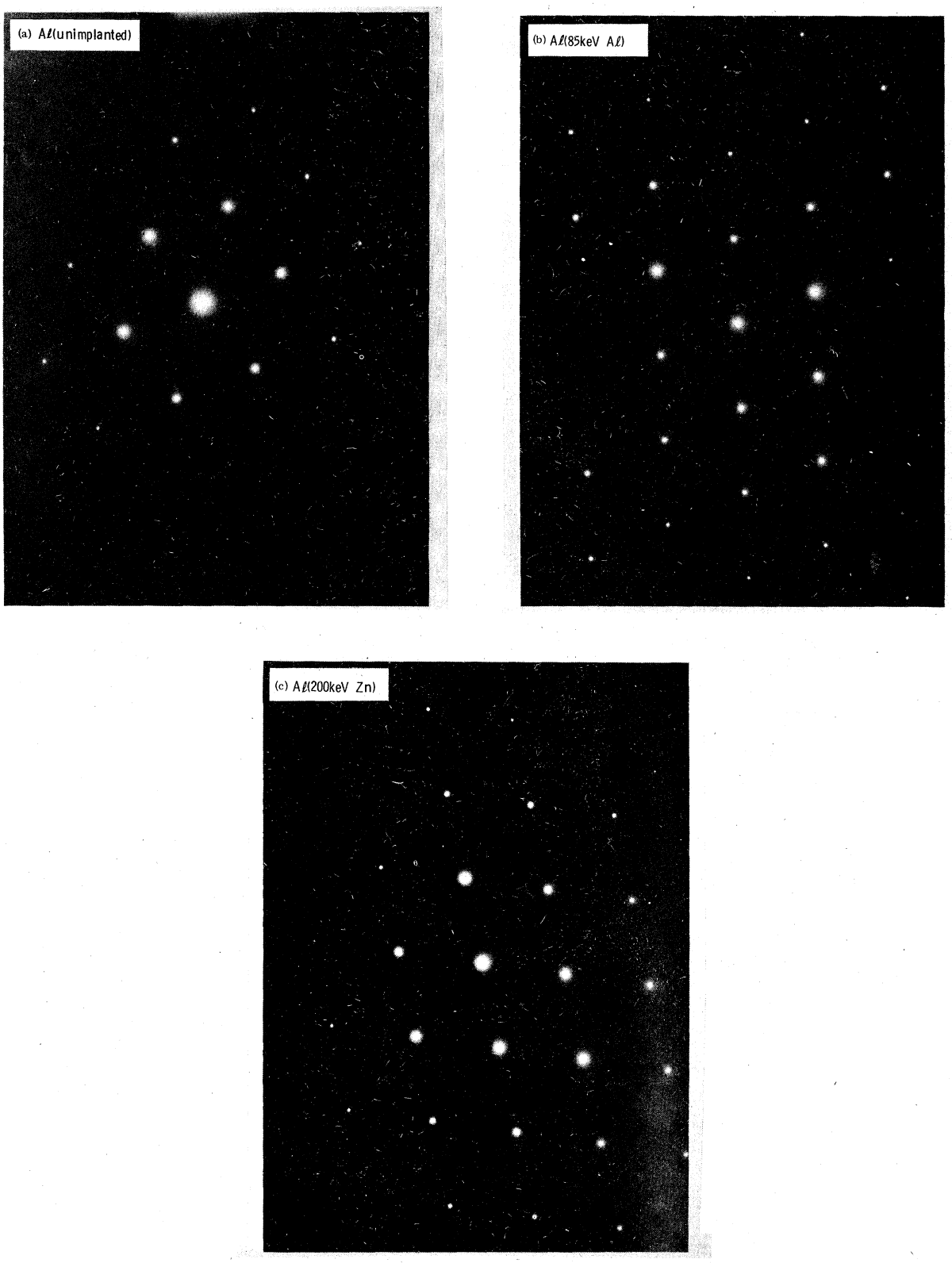

FIG. 13. Diffraction pattern for [110] direction for (a) virgin Al crystal, (b) Al-implanted Al crystal, and (c) Zn-implanted Al crystal.

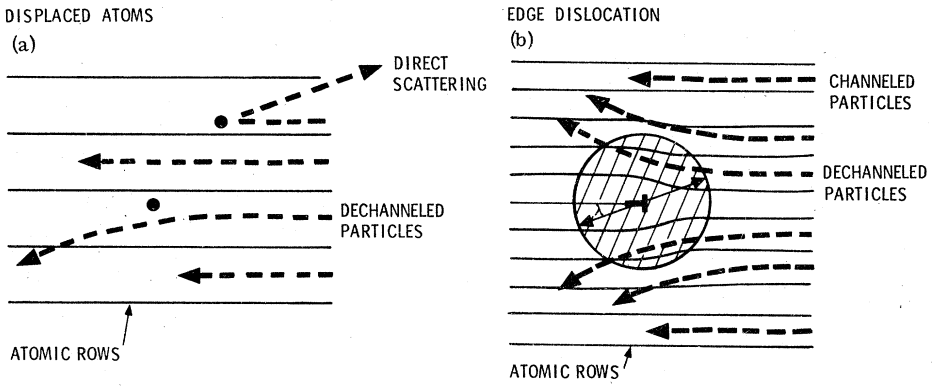

FIG. 14. Schematic of the processes of (a) direct scattering and dechanneling by displaced atoms and (b) dechanneling by a dislocation.

and $l(z)$ is the dislocation line length density at depth z. The dechanneling width λ is therefore defined by $N_D\sigma = L\lambda$.

From Eq. (3) we see that the function $[1-\chi_D(z)]/[1-\chi_V(z)]$ versus depth should become flat as depths corresponding to the undamaged region are reached. This is seen to be the case for the Al-implanted ⟨110⟩ axial data for several different He beam energies in Fig. 15. The depth z_1 of 1500 Å indicated in the figure corresponds to approximately the projected range plus range spread expected theoretically for 85-keV Al in Al. The break in the slope is seen to be somewhat below this depth, indicating that the disorder extends deeper than this. A second depth for analysis of the data of $z_2 = 4000$ Å has also been used, since by this depth the relative change in slope in Fig. 15 and all the other dechanneling data suggest that the entire region of implantation disorder has been sampled. Thus the value of $L(z)$ corresponding to the total amount of implantation disorder in the layer should be obtained.

In Fig. 16, the same analysis approach is applied to the {111} planar data for the Al implants. The

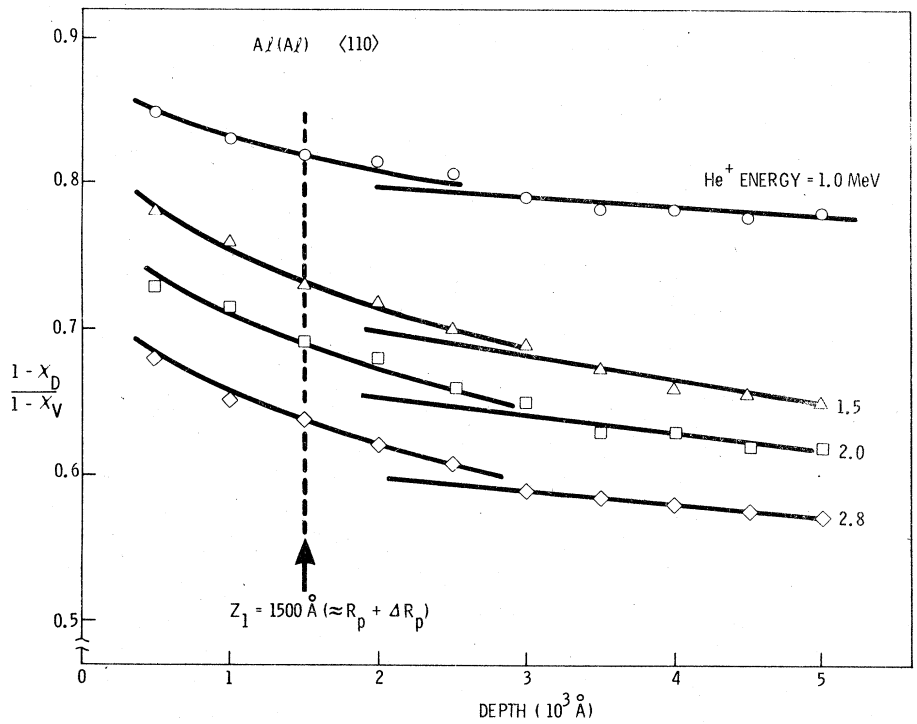

FIG. 15. Dechanneling parameter vs depth for Al-implanted Al as a function of He analysis energy for ⟨110⟩ axial channeling.

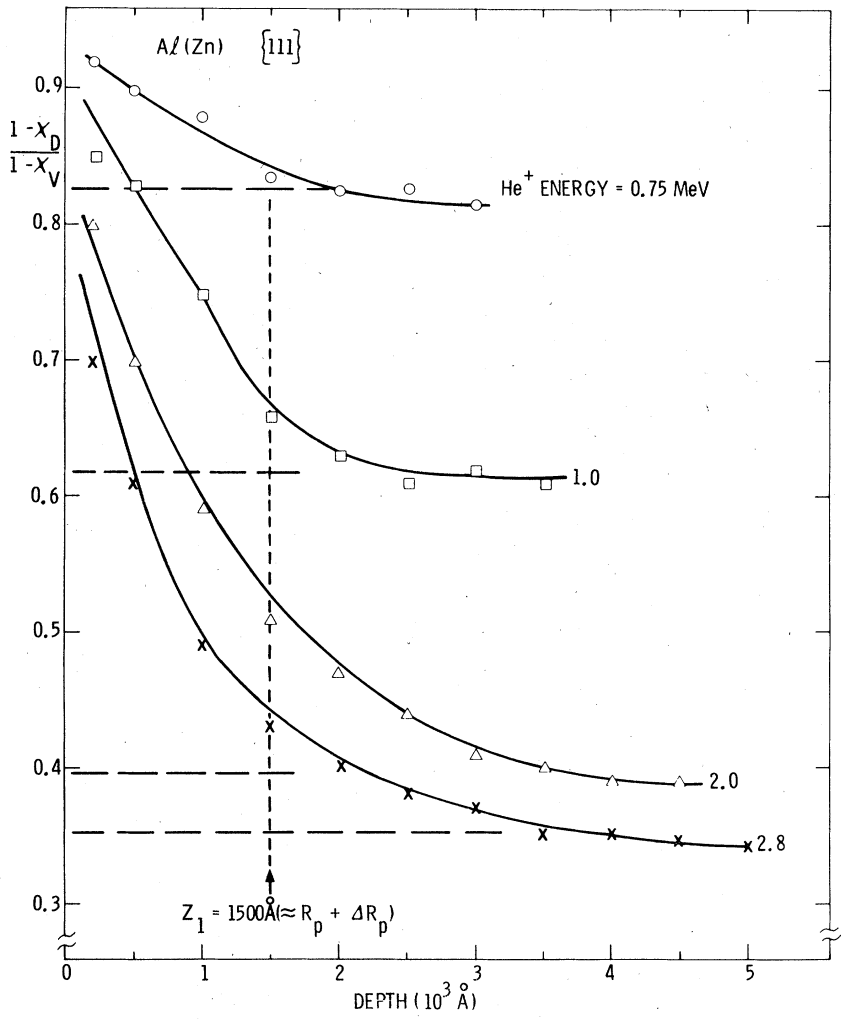

FIG. 16. Dechanneling parameter vs depth for Al-implanted Al as a function of He analysis energy for {111} planar channeling.

changes in slope are more apparent in the planar channeling analysis for all but the lowest analysis energy. This suggests that a more sensitive measure of the depth dependence of the dislocations is given by the planar channeling data.

One point of consistency throughout all the data, including the four different energies for axial channeling and the four different energies for planar channeling, is that the break in the slope, which indicates the dividing point between the disordered and undisordered regions of the crystal, occurs at the same depth in all cases. The $(1-\chi_D)/(1-\chi_V)$ value has not become a constant at deeper depths, particularly for the axial data, but continues to decrease slowly. This indicates that the transverse energy distribution of the channeled particles has been modified due to the defects present at shallower depths.

Based on previous theoretical analysis[17] and Monte Carlo calculations,[18] the cross section $\lambda L(z)$ is expected to have the following energy dependence for both the axial and planar cases:

$$\lambda L(z) = k(z) E^{1/2}, \tag{5}$$

where the parameter k is dependent upon the channeled particle and target parameters, as will be discussed later. To explore whether our experimental data follows the energy dependence predicted by Eqs. (3) and (5), in Fig. 17 we plot $\log[(1-\chi_D)/(1-\chi_V)]$ at the indicated depths versus $E^{1/2}$ for both the axial and planar Al-implanted Al data. As seen in Fig. 17, both the axial and planar data follow straight lines, indicating that the predicted energy dependence of Eq. (5) is obeyed experimentally. This is particularly convincing for the planar data for which the $(1-\chi_D)/(1-\chi_V)$ values change by nearly one order of magnitude between the highest and lowest beam

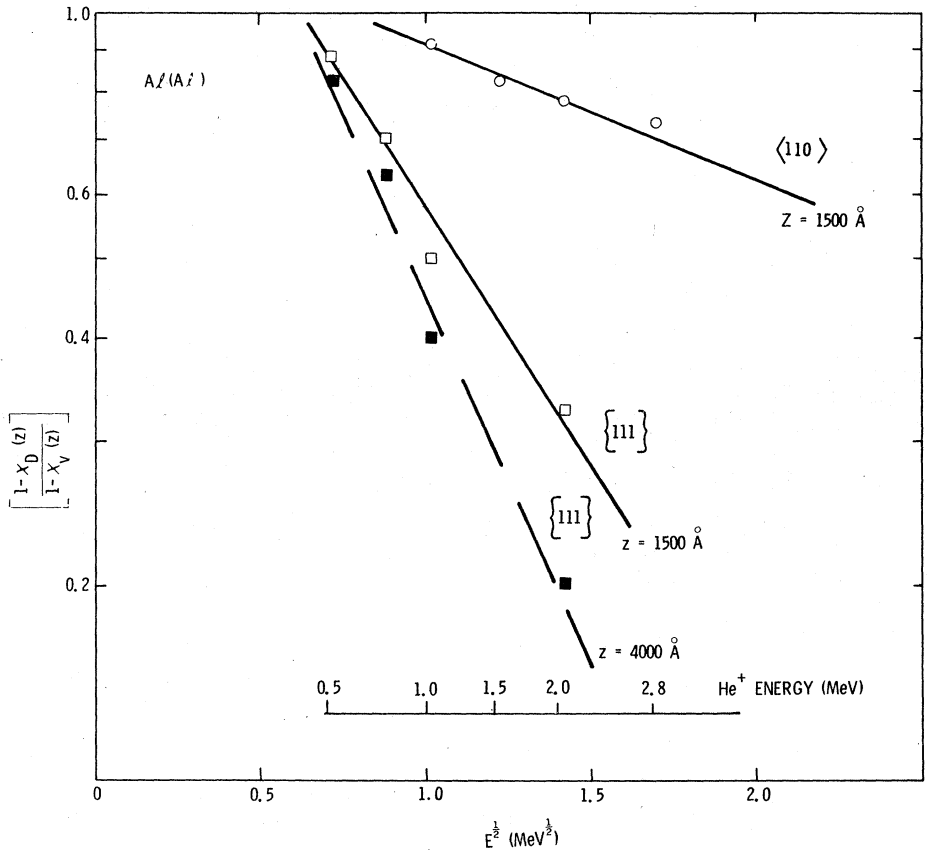

FIG. 17. Dechanneling parameter vs $E^{1/2}$ where E is the incident beam energy for He channeling along ⟨110⟩ axial and {111} planar directions taken at the depths, z, indicated.

energy. The data for the axial direction is also consistent with a $E^{1/2}$ dependence, although the values do not extend over a sufficiently large range to unambiguously eliminate other functional dependences. Since the energy dependence of Eq. (5) is obeyed to within experimental accuracy, then the slopes of the lines drawn through the data in Fig. 17 can be used to obtain the value of $k(z)$.

Based on Eqs. (3)–(5) and the consistency of the experimental observations with the predicted $E^{1/2}$ dependence for λ, all the experimental data were analyzed in terms of $(1-\chi_D)/(1-\chi_V)$ and fit to the exponential function $Ae^{-kE^{1/2}}$. A summary of all the data in terms of the extracted values for k and A is given in Table I. The k values are observed to be appreciably higher for planar channeling than for axial channeling as compared at a depth $z = 1500$ Å. The same trend has been found for the analysis at $z = 4000$ Å. The accuracy for the k values is estimated to be ± 0.02. The A values represent $(1-\chi_D)/(1-\chi_V)$ extrapolated to zero energy and in the axial case are near one, as predicted in this simple analysis, while in the planar case they differ considerably from 1. This is believed to result from our assumption of additivity for the dechanneling mechanisms present. A detailed description of the change in the transverse energy distribution with traversed depth would be required to account for both the deviation of A from 1 in the planar case and the continuing change of $(1-\chi_D)/(1-\chi_V)$ at depths deeper than the damaged region.

A comparison between H and He analysis along the ⟨110⟩ axial channeling direction for the Al-implanted samples at a depth of $z = 1500$ Å is given in Fig. 18. The data is plotted in the same way as in Fig. 17, except that the $(1-\chi_D)/(1-\chi_V)$ scale is plotted linearly for this region of small change and small value for the argument of the exponent, $k(z)E^{1/2}$. The data of Fig. 18 demonstrate the relatively good consistency between the He^+ and H^+ analysis, with the k value for proton analysis seen to be somewhat larger than that for He analysis, as given in Table I.

The analysis of the Zn-implanted Al data has been carried out in the same way, and the results give the same qualitative behavior as observed for Al-implanted Al. Figure 19 shows a plot of

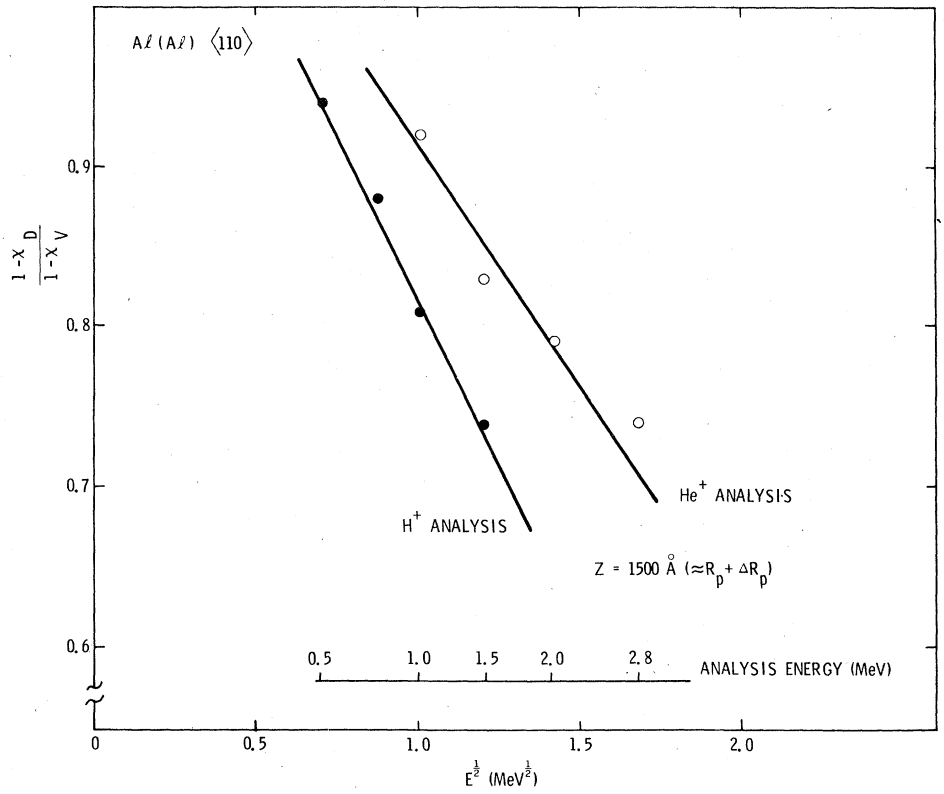

FIG. 18. Dechanneling parameter vs $E^{1/2}$ for Al-implanted Al for H and He analysis beams incident along the ⟨110⟩ axis.

$(1-\chi_D)/(1-\chi_V)$ versus depth for the (a) ⟨110⟩ axial and (b) {111} planar analysis as a function of He analyzing beam energy. Again, there is a rapid change in this damage parameter with depth followed by a region of constant slope after passing through the implantation-disordered region. Also, the planar data again show a more pronounced depth dependence than the axial data at the higher analysis beam energies, and the break point between the region of changing slope and of approximately constant slope is about the same in all the measurements.

One advantage of the Zn-implanted samples is that the final depth distribution of the implanted Zn is also measured in the ion backscatterihg measurements. Thus, in Fig. 20 is shown the observed Zn profile along with the 1-MeV He planar dechanneling data for the $(1-\chi_D)/(1-\chi_V)$ parameter. Since the theoretically predicted depth distribution[9] of the damaged deposition by the Zn ions is similar in shape and located slightly shallower than the Zn-ion profile, the Zn profile provides a measure of the maximum depth at which the damaged induced by the implant would be expected to have been initially deposited. The arrow indicates the calculated Zn ion $(R_p + \Delta R_p)$ value.

The Zn profile is seen to extend deeper than theoretically predicted, but does exhibit a fairly Gaussian shape, as would be predicted. For example, the projected range R_p is observed to be at $\simeq 1300$ Å in contrast to the predicted value of ≈ 1000 Å. The peak in the damaged deposition curve for this case occurs at ≈ 0.6 of the peak in the final implanted ion profile,[9] and this would correspond to ≈ 800 Å, which is near the center of the most rapid change in the damage parameter for 1-MeV He plotted in upper part of the curve. Thus, there is good correspondence in depth be-

TABLE I. Values of k and A extracted from the experimental data for Al-implanted Al as a function of axial or planar channeling direction, projectile type, and analysis depth.

Crystal direction	Channeled particle	Depth (Å)	A	k (MeV$^{-1/2}$)
⟨110⟩	He	1500	1.3	0.35
⟨110⟩	He	4000	1.2	0.37
⟨110⟩	H	1500	1.3	0.47
{111}	He	1500	2.3	1.38
{111}	He	4000	3.5	2.05

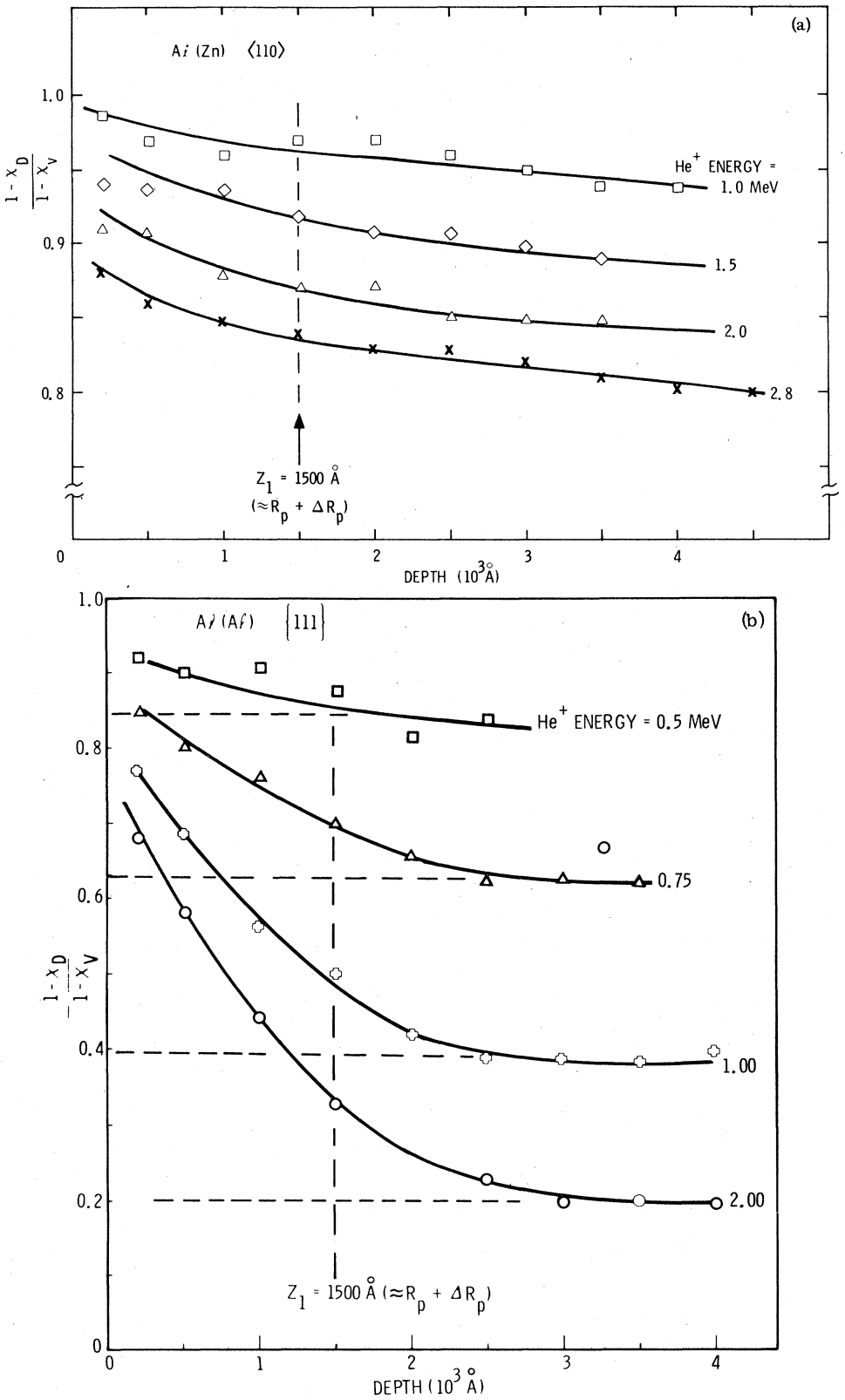

FIG. 19. Dechanneling parameter vs depth for Zn-implanted Al as a function of incident He energy along the (a) ⟨110⟩ axial and (b) {111} planar directions.

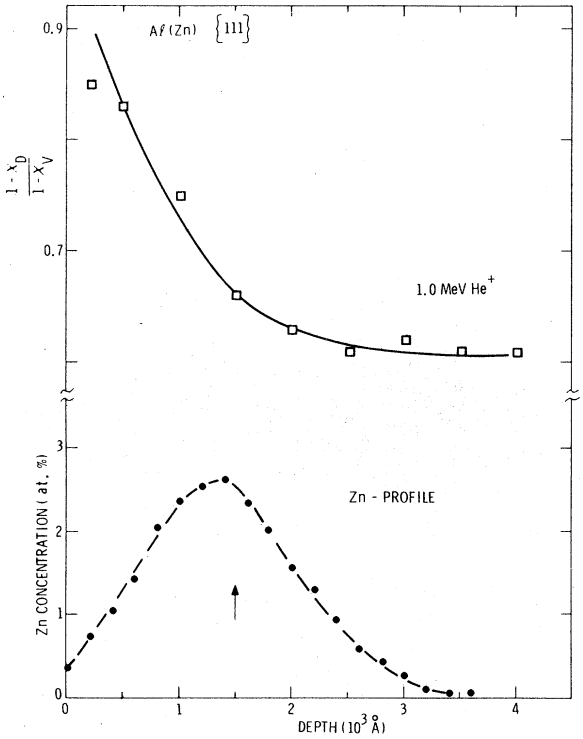

FIG. 20. Comparison of Zn concentration vs depth measured by ion backscattering with dechanneling parameter vs depth for 1-MeV He incident along the {111} planar direction in Zn-implanted Al.

tween the region of damage deposition as observed by the planar dechanneling analysis presented here and that which would be predicted from the observed Zn concentration profile.

The logarithm of the damage parameter versus $E^{1/2}$ is plotted for the Zn-implanted Al in Fig. 21. Again, the same general behavior is observed confirming the $E^{1/2}$ dependence. Extracted values for the parameters A and k for He channeling analysis at depths 1500 and 4000 Å are given in Table II. The data show the same trends as in the Al-implanted case.

From the total projected length of the dislocation lines L determined from the TEM measurements, we can obtain the dechanneling width λ given in

TABLE II. Values of k and A extracted from the experimental data for Zn-implanted Al.

Crystal direction	Channeled particle	Depth (Å)	A	k (MeV$^{-1/2}$)
⟨110⟩	He	1500	1.2	0.22
⟨110⟩	He	4000	1.2	0.23
{111}	He	1500	1.5	0.76
{111}	He	4000	1.8	1.01

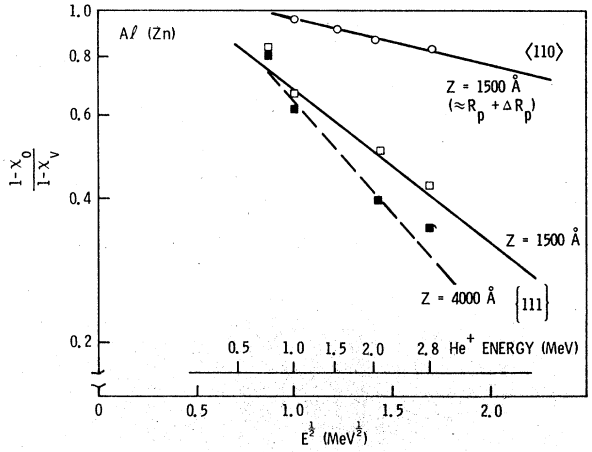

FIG. 21. Dechanneling parameter vs $E^{1/2}$ for Zn-implanted Al for He channeling along the ⟨110⟩ axial and {111} planar directions measured at the depth z indicated.

Eq. (5). The values of L obtained by the TEM measurements were $L = 1.6 \times 10^6$ cm/cm^2 for the Al-implanted samples and $L = 9.6 \times 10^5$ cm/cm^2 for the Zn-implanted samples. These numbers include the correction factors for the differences in sample tilting during implantation and the fraction of dislocations out of contrast. From geometrical considerations, the actual length is greater than the projected length by a factor ≈1.27. Using the above L values we obtain the experimentally-determined values of the dechanneling width for dislocations. These are given in Table III based on the k values taken at $z = 1500$ Å. The depth at which the k values should be compared to the L value determined by TEM is not precisely determined in the present measurements. However, since the TEM samples were tilted 45° during implantation, the depth of $z = 1500$ Å in the channeling samples corresponds to ~1000 Å in the TEM samples, which is the approximate depth that was sampled in the

TABLE III. Comparison of experimentally measured and theoretically predicted dechanneling widths λ in angstroms for beam energy E in MeV at $z = 1500$ Å ($\approx R_p + \Delta R_p$).

Direction	Channeled particle	Implanted Ion	Experiment	Theory
Axial ⟨110⟩	He	Al	$22E^{1/2}$	$21E^{1/2}$
	H	Al	$29E^{1/2}$	$30E^{1/2}$
	He	Zn	$23E^{1/2}$	$21E^{1/2}$
Planar {111}	He	Al	$85E^{1/2}$	$79E^{1/2}$
	He	Zn	$79E^{1/2}$	$79E^{1/2}$

micrographs. In the extreme limit if all the damage as measured by He channeling at $z = 4000$ Å were sampled in the TEM measurements, then the values of λ would be $23E^{1/2}$ and $24E^{1/2}$ for $\langle 110 \rangle$ analysis, and $127E^{1/2}$ and $105E^{1/2}$ for $\{111\}$ analysis, for Al-implanted and Zn-implanted Al, respectively. Although the planar channeling results are more sensitive than the axial channeling results to this choice of z, the results are still within the estimated accuracy of a factor of 2 for the absolute value of L. Also, the dislocations in the implanted Al were of mixed type and orientation, and thus the experimental dechanneling widths of Table III represent averages over these parameters.

V. DISCUSSION

Transmission electron microscopy measurements have indicated that Al and Zn-implanted single crystal Al samples have large densities of dislocations in the implanted region. From the TEM measurements, as well as the consistency of the dechanneling measurements, it is concluded that dislocations are the dominant type of defect giving rise to the observed dechanneling. Therefore, these implanted samples are used as a model system to investigate the influence of dislocations on dechanneling, and thereby to further develop the ion channeling-backscattering technique for the analysis of this type of disorder.

Detailed dechanneling measurements as a function of incident particle energy, particle type, and axial or planar channeling direction gave well-defined dependences consistent with the simple dechanneling analysis. The results indicate an $E^{1/2}$ dependence of the dislocation cross section for dechanneling (dislocation width) for both axial and planar channeling. The dislocation cross section is observed to be a factor of ≈ 4 higher for planar dechanneling than for axial dechanneling. Also, the axial dechanneling cross section is higher for protons than that for He particles of the same kinetic energy.

The expected behavior for dechanneling by dislocations has been considered theoretically by Quéré[17] in a simple analytical model and by Morgan and Van Vliet,[18] based largely on Monte Carlo calculations. Both the analytical and computer simulation studies predict an $E^{1/2}$ dependence for the dechanneling cross section, as is observed here experimentally. Quéré derives an analytical expression for the dechanneling cross section for dislocation lines from a model based on the curvature induced in the channels by dislocations. For axial channeling and averaging over all the possible orientations of the dislocation with respect to the axial channel direction, he obtains

$$\lambda_a = (b d a_{TF} E / \alpha Z_1 Z_2 e^2)^{1/2}, \tag{6}$$

where b is the length of the Burger's vector of the dislocation, d is the average interatomic spacing along the rows forming the channel, a_{TF} is the Thomas-Fermi screeing distance, e the electronic charge, E the energy, Z_1 the incident particle atomic number, Z_2 the average atomic number of the target atoms, and α is a constant for a given type dislocation and equals 12.5 and 4.5 for screw and edge dislocations, respectively.[17] In the implanted samples studied here dislocations of mixed type are present and we have used $\alpha \approx 8.5$.

For the $\langle 110 \rangle$ axial direction in Al Eq. (6) gives

$$\lambda_{\langle 110 \rangle} = 30(E/Z_1)^{1/2}, \tag{7}$$

where we have taken $b = 2.86$ Å, and λ and E are in units of angstroms and MeV, respectively. The value of $(a_{TF})^{1/2}$ here is assumed to be constant with Z_1 for small Z_1. The theoretical agreement with our experimental observations (See Figs. 17, 18, 21, and Table III) is quite good, both in functional form and absolute magnitude. Such agreement is particularly satisfactory in view of the simple theoretical description used and the combined accuracy of the experimental measurements involved. Also, the correct trend is observed between He and H projectiles. For example, in comparing the consistency between our experimental measurements for the cross section for H and He with that theoretically predicted, we obtain 1.35 for the ratio $\lambda(\mathrm{H})/\lambda(\mathrm{He})$, while the value 1.4 is predicted theoretically.

For planar dechanneling Quéré gives[17]

$$\lambda_p = (b E / 8.6 Z_1 Z_2 e^2 N_p)^{1/2}, \tag{8}$$

where N_p is the atom density of the planes. This gives for He ions incident along the $\{111\}$ planar direction in Al

$$\lambda_{\{111\}} = 79E^{1/2}, \tag{9}$$

where λ and E are in units of angstroms and MeV, respectively. Again, we obtain relatively good agreement between experiment and theory (See Figs. 17 and 21 and Table III), with the better agreement given for the λ value determined experimentally at depth $z = 1500$ Å than at 4000 Å (see Sec. IV and Table III). One may also compare the experimental and theoretical ratio between the dechanneling cross section for $\{111\}$ planar and $\langle 110 \rangle$ axial dechanneling which ranges between 3.3 and 5.8 experimentally versus the calculated value of 3.7. The larger planar dechanneling cross section relative to that for axial dechanneling can be understood simply in terms of the planar potential being weaker than the row potential. The

dechanneling widths for the axial and planar case are 21 and 79 Å, respectively, for 1-MeV He. These large values compared with the axial or planar lattice width help to justify the above simple treatment of dislocation dechanneling, which does not require a detailed description of the particle trajectories in the vicinity of the dislocation. The agreement here and the relatively strong dependence of the experimental planar λ values on the depth of analysis is probably limited by the modification of the transverse energy distribution in the highly disordered region, which changes the subsequent dechanneling behavior of the beam.

Information on the depth distribution of dislocations is contained in the plot of the damaged parameter $(1-\chi_D)/(1-\chi_V)$ versus depth. From Eq. (3) it can be seen that the rate of change of this parameter with depth is closely related to the density of dislocations at a given depth. The present study has shown that the planar dechanneling data could potentially give a better measure of the depth distribution of the dislocation density than the axial channeling data. The results are consistent with what would be expected theoretically based on the observed Zn depth profile.

The present results indicate that a high density of dislocations is required for detection by dechanneling measurements. In our case the dislocation density in the implanted region is approximately 10^{11} cm length of line/cm^3 (=lines/cm^2). This density, which is introduced by only moderately high implantation fluences, is comparable to that found in cold-worked metals. We can estimate from these measurements that a minimum dislocation density of approximately 10^9–10^{10} lines/cm^2 is required for detection by single alignment channeling measurements.

ACKNOWLEDGMENTS

TEM measurements by R. A. Kant and participation by R. A. Kant and P. Baeri in parts of the earlier phases of this work are gratefully acknowledged. Experimental assistance was provided by C. Fuller, G. Harper, and V. Scuderi. This work was supported in part by the U. S. Department of Energy under Contract No. AT(29-1)789.

[1]J. W. Mayer, L. Eriksson, and J. A. Davies, *Ion Implantation in Semiconductors* (Academic, New York, 1971), Chap. 3.

[2]F. H. Eisen, *Channeling*, edited by D. V. Morgan (Wiley, New York, 1973), Chap. 14.

[3]G. Foti, P. Baeri, E. Rimini, and S. U. Campisano, J. Appl. Phys. 47, 5206 (1976).

[4]P. P. Pronko and K. L. Merkle, *Applications of Ion Beams to Metals*, edited by S. T. Picraux, E. P. EerNisse, and F. L. Vook (Plenum, New York, 1974), p. 481; P. P. Pronko, Nucl. Instrum. Methods 132, 249 (1976).

[5]S. U. Campisano, G. Foti, E. Rimini, and S. T. Picraux, Nucl. Instrum. Methods 149, 371 (1978).

[6]Y. Quéré, J. Nucl. Mater. 53, 262 (1974).

[7]E. Rimini, S. U. Campisano, G. Foti, P. Baeri, and S. T. Picraux, *Ion Beam Surface Layer Analysis*, edited by O. Meyer, G. Linker, and F. Käppeler (Plenum, New York, 1976), p. 597.

[8]G. Foti, S. T. Picraux, S. U. Campisano, E. Rimini, and R. A. Kant, *Ion Implantation in Semiconductors, 1977*, edited by F. Chernow, J. A. Borders, and D. K. Brice (Plenum, New York, 1977), p. 247.

[9]D. K. Brice, *Ion Implantation Range and Energy Deposition Distributions* (Plenum, New York, 1975), Vol. 1; and private communication.

[10]See *Ion Beam Handbook for Materials Analysis*, edited by J. W. Mayer and E. Rimini (Academic, New York, 1977).

[11]E. Lugujjo and J. W. Mayer, Phys. Rev. B 7, 1782 (1973).

[12]P. Sigmund and K. B. Winterbon, Nucl. Instrum. Methods 119, 541 (1974).

[13]E. Bøgh, Can. J. Phys. 46, 653 (1968).

[14]N. Matsunami and N. Itoh, *Atomic Collisions in Solids*, edited by S. Datz, B. R. Appleton, and C. D. Mook (Plenum, New York, 1975), p. 175.

[15]S. U. Campisano, G. Foti, F. Grasso, and E. Rimini, *Atomic Collisions in Solids*, edited by S. Datz, B. R. Appleton, and C. D. Mook (Plenum, New York, 1975), p. 905.

[16]M. L. Swanson, L. M. Howe, and A. F. Quenneville, Radiat. Eff. 25, 61 (1975).

[17]Y. Quéré, Phys. Status Solidi 30, 713 (1968); J. Mory and Y. Quéré, Radiat. Eff. 13, 57 (1972).

[18]D. V. Morgan and D. Van Vliet, *Atomic Collision Phenomena in Solids*, edited by D. W. Palmer, M. W. Thompson, and P. D. Townsend (North-Holland, London, 1970), p. 476.

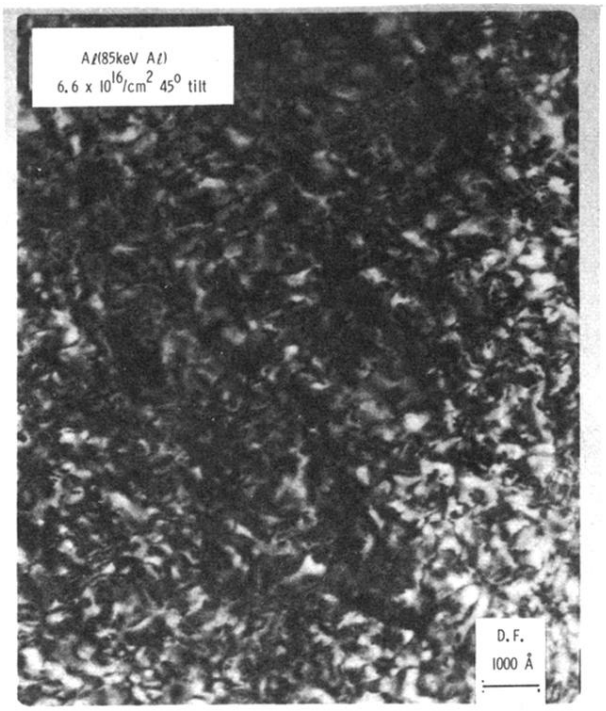

FIG. 11. Dark-field (D.F.) micrograph of Al-implanted Al using $g = [111]$.

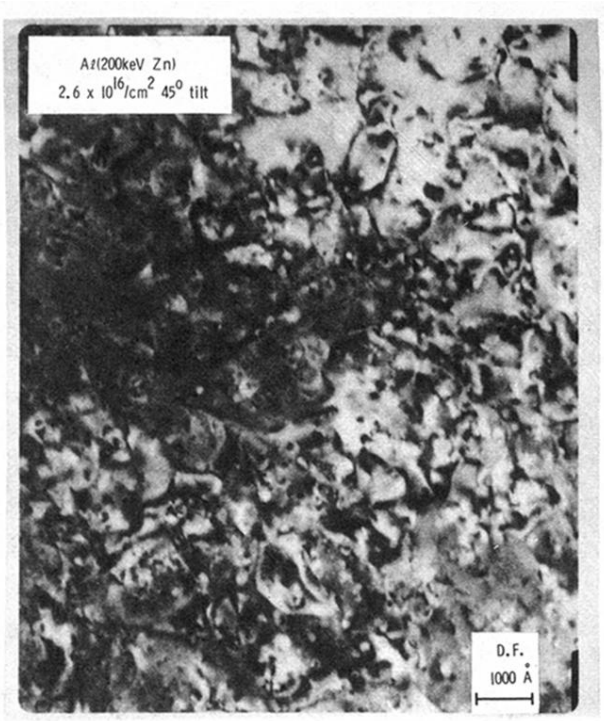

FIG. 12. Dark-field micrograph of Zn-implanted Al using $g = [111]$.

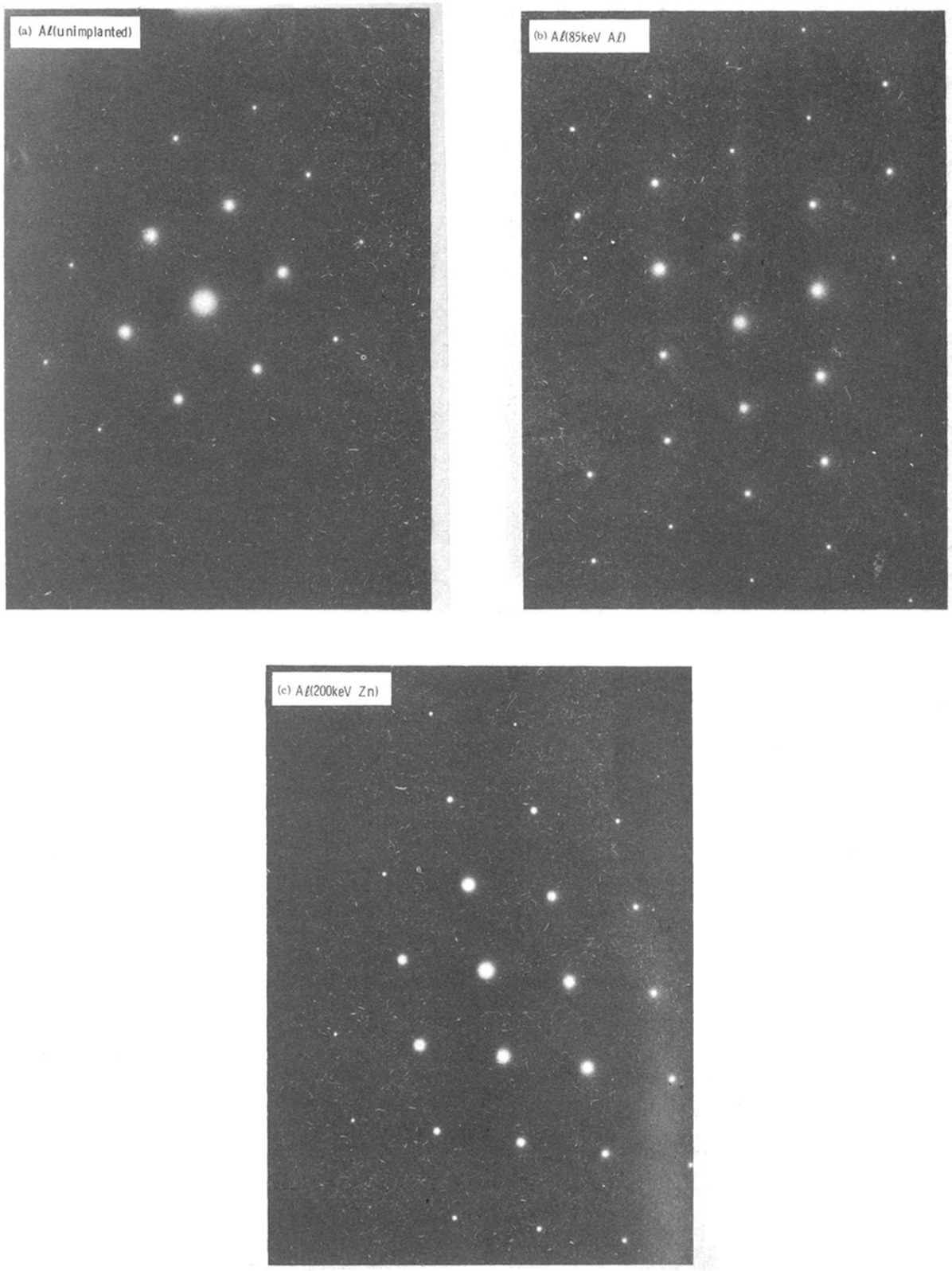

FIG. 13. Diffraction pattern for [110] direction for (a) virgin Al crystal, (b) Al-implanted Al crystal, and (c) Zn-implanted Al crystal.